A new X-ray spectrometer for high-resolution Compton profile measurements at SPring-8

N. Hiraoka,[a]*† M. Itou,[b] T. Ohata,[b] M. Mizumaki,[b] Y. Sakurai[b] and N. Sakai[a]

[a]Himeji Institute of Technology, Kouto 1-2-3, Kamigori, Ako, Hyogo 678-1297, Japan, and [b]Japan Synchrotron Radiation Research Institute (JASRI), SPring-8, Kouto 1-1-1, Mikazuki, Sayo, Hyogo 679-5198, Japan. E-mail: hiraoka@spring8.or.jp

An X-ray spectrometer for high-resolution Compton profile measurements using 90–120 keV X-rays has been designed and constructed at SPring-8. A Cauchois-type triply layered bent-crystal analyzer was employed for the energy analysis. A novel use of a solid-state detector with a large active area was devised as a position-sensitive detector. A resolution of 0.10 atomic units in electron momentum has been achieved at an incident X-ray energy of 115 keV. A Compton profile of a single crystal of Nb was measured with a counting rate of 30 counts s^{-1} at the Compton peak, which demonstrates that the spectrometer is capable of measuring Compton profiles of heavy-element materials.

Keywords: high-energy X-rays; Cauchois-type spectrometers; Compton profiles; electron momentum density.

1. Introduction

An energy profile of Compton-scattered X-rays contains information about the electron momentum density distribution, which is expressed as

$$J(p_z) = \iint n(\mathbf{p})\, \mathrm{d}p_x\, \mathrm{d}p_y, \tag{1}$$

where $n(\mathbf{p})$ is the ground-state electron momentum density. Hence, the Compton scattering technique has been widely applied to various kinds of materials in order to study their electronic structures and bonding mechanisms in terms of the momentum space (see, *e.g.*, Williams, 1977).

Recent developments of synchrotron radiation sources have made it possible to use a crystal analyzer for high-resolution and highly accurate measurements. Since the first Cauchois-type high-resolution Compton scattering spectrometer was constructed at LURE (Loupias & Petiau, 1980), the same type of spectrometers using higher-energy incident X-rays have been built in the wiggler beamlines at KEK-PF (Shiotani *et al.*, 1989), HASYLAB (Berthold *et al.*, 1992) and KEK-AR (Sakurai *et al.*, 1992). In parallel to these, a scanning Johann-type spectrometer was also constructed at the ESRF (Suortti *et al.*, 1999). At the APS, furthermore, a scanning inverse-Cauchois-type spectrometer is being developed for high-energy X-ray spectroscopies (S. D. Shastri & D. R. Haeffner, private communication). The Cauchois-type spectrometer has the advantage that the energy resolution is hardly affected by the effective beam size on the sample. Hence, a thicker sample can be used in order to obtain a higher counting rate by fully utilizing the penetrating power of high-energy X-rays.

We report a Cauchois-type spectrometer designed and constructed at BL08W of SPring-8. It operates with 90–120 keV incident X-rays, making it possible to obtain Compton profiles of virtually all materials. The following section describes some details of the spectrometer, together with a discussion on the focal width of a bent Laue crystal. The performance is given in §3, and the summary and conclusions are described in the final section. The reader is referred to Sakurai (1998) and Yamaoka *et al.* (1998, 2000) for details of the beamline and the monochromator.

2. Spectrometer

2.1. *Basic design and layout*

In a Cauchois-type spectrometer, a bent-crystal analyzer and a position-sensitive detector (PSD) are both located on a Rowland circle. The crystal analyzes the energy of the Compton-scattered X-rays in the transmission geometry before the scattered X-rays reach the PSD. The energy of the Compton-scattered X-rays is converted into electron momentum by the following equation (Eisenberger & Reed, 1974),

$$p_z = mc\frac{\omega_2 - \omega_1 + \omega_1\omega_2\,(1-\cos\theta)/mc^2}{(\omega_1{}^2 + \omega_2{}^2 - 2\omega_1\omega_2\cos\theta)^{1/2}}. \tag{2}$$

Here, p_z is the electron momentum, ω_1 is the energy of incident X-rays, ω_2 is that of the Compton-scattered X-rays, θ is the scattering angle, m is the rest mass of the electron, and c is the velocity of light. The momentum resolution, Δp_z, is approximately given by the following relation (Shiotani *et al.*, 1989),

$$\Delta p_z = \left[\left(\frac{\partial p_z}{\partial \omega_1}\Delta\omega_1\right)^2 + \left(\frac{\partial p_z}{\partial \omega_2}\Delta\omega_2\right)^2 + \left(\frac{\partial p_z}{\partial \theta}\Delta\theta\right)^2\right]^{1/2}. \tag{3}$$

Here, $\Delta\omega_1$ is the bandwidth of the monochromator, $\Delta\omega_2$ is the energy resolution of the spectrometer, and $\Delta\theta$ is the spread of the Compton scattering angle. With $\omega_1 = 115$ keV, $\theta = 165^\circ$ and $\omega_2 = 80.2$ keV (the Compton peak energy), one obtains the following numerical values from (2),

$$\partial p_z/\partial\omega_1 = 0.4919 \ \text{[a.u./keV]}, \tag{4}$$

$$\partial p_z/\partial\omega_2 = 1.023 \ \text{[a.u./keV]},$$

$$\partial p_z/\partial\theta = 3.310 \ \text{[a.u./rad]}.$$

† Present address: Japan Synchrotron Radiation Research Institute (JASRI), SPring-8, Kouto 1-1-1, Mikazuki, Sayo, Hyogo 679-5198, Japan.

Table 1
Overall momentum resolution and each contribution in equation (3).

$\Delta\omega_1$, $\Delta\omega_2$ and $\Delta\theta$ are the bandwidth of the monochromator, the energy resolution of the spectrometer, and the spread of the scattering angle, respectively. $(\partial p_z/\partial\omega_1)\Delta\omega_1$, $(\partial p_z/\partial\omega_2)\Delta\omega_2$ and $(\partial p_z/\partial\theta)\Delta\theta$ denote their contributions to the overall momentum resolution Δp_z. Slit size is denoted by width × height.

Crystal thickness (mm)	Slit size (mm^2)	$\Delta\omega_1$ (eV)	$(\partial p_z/\partial\omega_1)\Delta\omega_1$ (a.u.)	$\Delta\omega_2$ (eV)	$(\partial p_z/\partial\omega_2)\Delta\omega_2$ (a.u.)	$\Delta\theta$ (rad)	$(\partial p_z/\partial\theta)\Delta\theta$ (a.u.)	Δp_z (a.u.)
1.0	0.2×20	113	0.055	80	0.082	0.003	0.01	0.10

The spread of the scattering angle $\Delta\theta$ is mainly caused by the effective beam size on the sample and the thickness of the analyzer crystal. In the present case, however, the contribution of $\Delta\theta$ to Δp_z is negligibly small (see Table 1). To make the overall momentum resolution better than 0.1 a.u. with $\Delta\omega_1$ = 115 eV at 115 keV, we find from equations (3) and (4) that $\Delta\omega_2$ should be better than 80 eV.

We have chosen the Si 620 reflection, which leads to an energy resolution $\Delta\omega_2$ of 48 eV $\simeq$ 96 eV, *i.e.* an overall momentum resolution of 0.07 a.u. $\simeq$ 0.11 a.u. for ρ = 3650 mm, Δx = 200 µm $\simeq$ 400 µm, where ρ is the distance between the analyzer and the PSD, and Δx is the spatial resolution of the PSD. A triply layered bent-crystal analyzer is employed for the energy-analyzing device to obtain higher detection efficiency. Details of the analyzer are given in §2.2.

Concerning the PSD, a gas-filled counter and an imaging plate are commercially available, but these are unpractical for X-rays above 70 keV due to poor detection efficiencies. Furthermore, both PSDs have no energy resolution, which causes some difficulties in determining the background noise in the actual measurements. Therefore, we have to give up on using a commercially available PSD. Our novel idea is that a large-active-area Ge SSD with some slits in front can be used as a PSD. We use a Ge-SSD with a diameter of 50 mm and attach to it four 200 µm-wide Ta slits with an interval of 10 mm. The interval corresponds to an energy difference of ~2.5 keV on the present Rowland circle, which is beyond the energy resolution of the Ge-SSD. Therefore, we can simultaneously accumulate the events at four different p_z points. The Ge-SSD and the slits (henceforth we call this the quasi-PSD) are mounted on a movable stage to scan the energy range 70–90 keV.

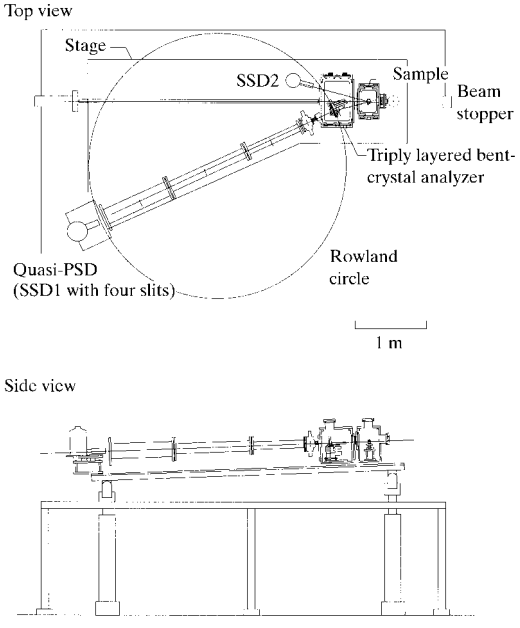

Figure 1
Layout of the spectrometer.

A schematic drawing of the spectrometer is shown in Fig. 1. The distances between the sample and the analyzer and between the analyzer and the quasi-PSD are 500 mm and 3650 mm, respectively. In order to reduce the background noise from the analyzer (Sakurai *et al.*, 1992), we insert vertical and horizontal slits of 3 mm-thick Ta at the point where all the signal paths cross. Furthermore, most of the X-ray beam path is evacuated to reduce scattering by air. A Ge solid-state detector (SSD2 in Fig. 1) monitors the flux of the incident X-rays.

2.2. *Analyzer*

2.2.1. *Focal width of monochromatic X-rays by bent Laue crystal* The bending inevitably produces a deformation of a volume element in the crystal, which changes the spacing and the direction of diffraction planes throughout the crystal. Both changes affect the focus on the Rowland circle. The focusing properties of a bent Laue crystal have been extensively discussed by Suortti & Thomlinson (1988) and Suortti *et al.* (1994) for an elastically isotropic crystal, and by Schulze *et al.* (1998) for an anisotropic crystal. For the isotropic crystal case, Suortti *et al.* (1994) present the relation between the minimum focal width and the crystal thickness for a parallel and narrow beam of white X-rays. However, no expression is given for the focal width of monochromatic X-rays diverging from a point source. Here, we briefly describe this in connection with the resolution of the spectrometer.

The present geometry is shown in Fig. 2. X-rays with a given wavelength λ emitted from a point source S are diffracted at M in the crystal before arriving at F on the PSD. From the simple geometrical consideration (see Appendix A), it is found that the position y is given as

$$y = [(\rho + t)\cos\alpha + n]\tan(\theta_B - \chi + \alpha) - (\rho + t)\sin\alpha. \quad (5)$$

Here, ρ is the bending radius of the neutral surface NS in the bent crystal, t is the distance between M and NS, θ_B is the

Bragg angle for X-rays with wavelength λ, and χ is the angle between the surface normal of the crystal and the Bragg diffraction planes. α is given as the angle MOM_o, where M_o and O are the diffracting position on NS and the focal position on the Rowland circle, respectively, for X-rays with the Compton peak energy. n is the distance between O on the Rowland circle and O' on the PSD.

To consider the effects of the deformation by bending, we assume that the crystal plate is elastically and isotropically deformed. As we show in Appendices B and C, α, θ_B and χ are written as

$$\alpha = (\theta_B - \theta_{Bo}) + (\chi - \chi_o) - \big(\arcsin\{[(\rho + t)/q]\sin(\theta_B + \chi)\} - \arcsin[(\rho/q)\sin(\theta_{Bo} + \chi_o)]\big), \quad (6)$$

$$\theta_B = \arcsin\big(\lambda/\{2d[1 + (t/\rho)(\cos^2\chi_o - \nu\sin^2\chi_o)]\}\big), \quad (7)$$

$$\chi = \chi_o + (t/2\rho)(1 + \nu)\sin 2\chi_o, \quad (8)$$

and

$$q = [\rho^2 + \ell^2 + 2\rho\ell\cos(\theta_{Bo} + \chi_o)]^{1/2}, \quad (9)$$

where θ_{Bo} is the Bragg angle of the Compton peak X-rays for non-deformed Si 620 planes and χ_o is the angle between the surface normal of the crystal and the non-deformed Si 620 planes. The non-deformed condition in the bent crystal is fulfilled on NS. ν is the Poisson ratio, d is the spacing of the non-deformed Si 620 planes and ℓ is the distance between S and M_o. q is the distance between S and O.

Once λ is given, the landing position y on the PSD has a one-on-one connection to t, since α, θ_B and χ are uniquely determined by t. Fig. 3 shows the relation between y and t for X-rays of 80.2 keV (the Compton peak energy) and $n = 0$. The Bragg-diffracted X-ray beams at this energy are almost normal to the crystal surface; that is the geometrical condition for the smallest parallax and best focusing (Cauchois, 1932). Even so, the focal width w increases with an increase of the crystal thickness T for the zero absorption approximation, since y varies monotonously with t, where w and T are defined as a span of y and t, respectively.

2.2.2. *Triply layered bent-crystal analyzer* As shown in Fig. 3, a crystal thickness of 1 mm gives a focal width of 200 µm. Convoluting this with the spatial resolution of the PSD, Δx = 200 µm $\simeq$ 400 µm, the overall energy resolution of the spectrometer is expected to be $\Delta\omega_2$ = 48 eV $\simeq$ 96 eV. However, the thickness of 1 mm is too thin to obtain a high detection efficiency for 80 keV X-rays, since at this energy the absorption length becomes 10 mm. Therefore, we stack three identically bent crystals of thickness 1 mm into a triply layered bent-crystal analyzer to attain an efficiency which is as high as possible.

Fig. 4 shows the analyzer assembly. Each crystal has a triangular shape, 30 mm at the base and 110 mm in height. The base of the crystal is fixed to each holder and a micrometer screw-head pushes the apex A to bend the crystal. The radius of curvature is adjusted to 3650 $\pm$ 20 mm by using the optical method (Shiotani *et al.*, 1989). After the crystals are bent, the holders are assembled on the analyzer frame. The orientations of the bent crystals are adjusted to coincide with each other by turning each crystal holder about the pivot P.

Since the identically bent crystals are stacked 5 mm apart from each other, two of the crystals do not share the Rowland

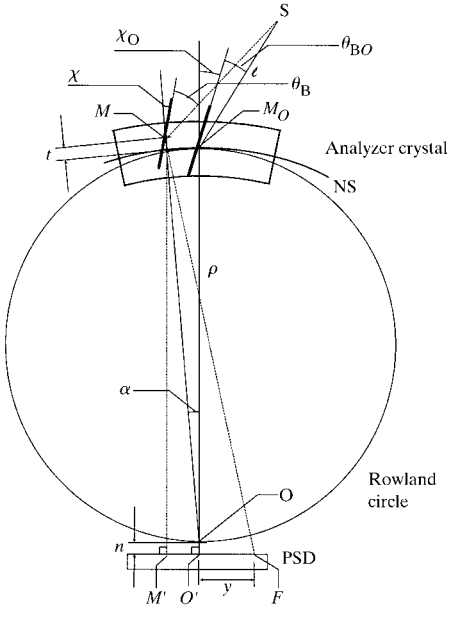

Figure 2
Focusing geometry for a cylindrically bent Laue crystal.

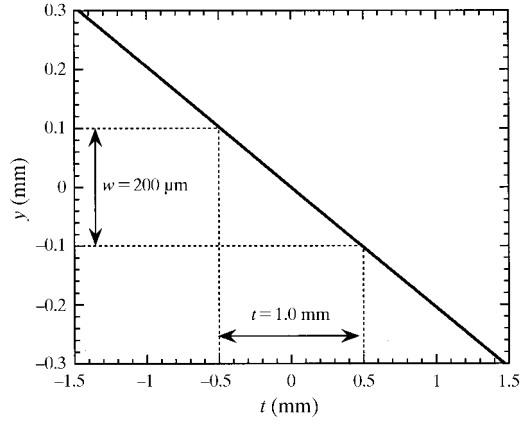

Figure 3
Relation between y and t for X-rays of 80.2 keV (Compton peak energy) and n = 0. Here, y is the landing position on the position-sensitive detector (PSD), t is the distance between the diffracting position M and the neutral surface NS, and n is the distance between O on the Rowland circle and O' on the PSD (see Fig. 2). A crystal thickness T of 1 mm gives a focal width w of 200 µm.

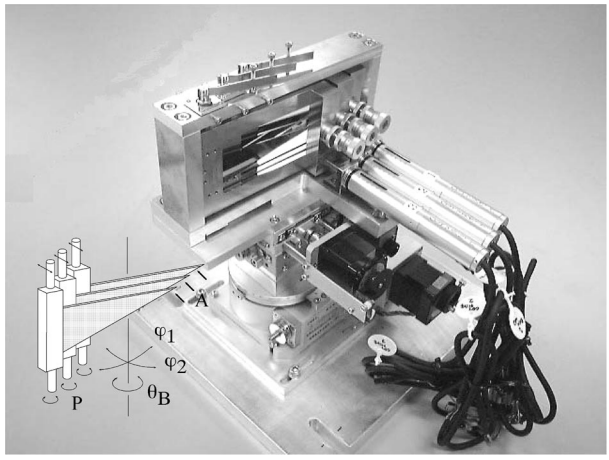

Figure 4
Photograph of the triply layered bent-crystal analyzer. The inset shows its schematic representation. The radius of curvature is adjusted by pushing apex A of each crystal, and parallelism between the crystals is adjusted by turning each holder about the pivot P. The frame on which the holders are mounted can be tilted along two directions (φ_1 and φ_2) and rotated to adjust the Bragg angle (θ_B).

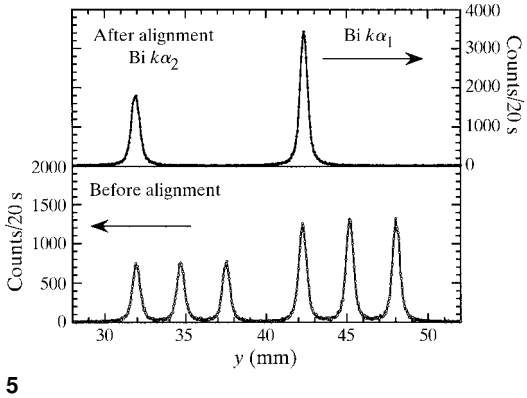

Figure 5
Energy profiles of Bi-$K\alpha_{1,2}$ fluorescence lines measured before alignment (lower frame) and after alignment (upper frame). Three pairs of $K\alpha_1$ and $K\alpha_2$ lines converge into one pair after alignment.

circle with the PSD. They correspond to the case of $n \neq 0$ in equation (5). The present arrangement of the bent crystals causes another broadening of the focus on the PSD. However, the effect is negligibly small.

In order to demonstrate the functioning of the triply layered bent-crystal analyzer, we measured energy profiles of Bi-$K\alpha_{1,2}$ lines (77.1 keV and 74.8 keV) before and after alignment of the crystals. As shown in Fig. 5, before alignment three pairs of $K\alpha_1$ and $K\alpha_2$ lines appear (the lower frame), after alignment they converge into one pair (the upper frame). The integrated intensity of these peaks are about three times higher than those before alignment, but the width of them remains the same. The results indicate that the detection efficiency has been successfully enhanced without any deterioration of the resolution.

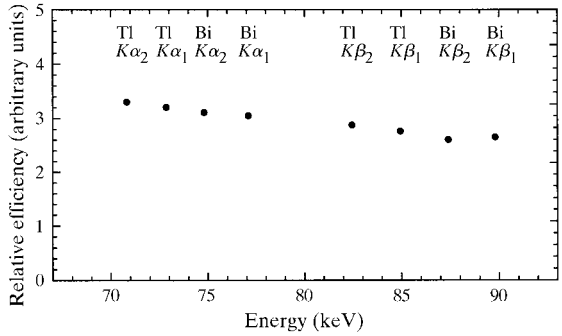

Figure 6
Detection efficiency of the triply layered bent-crystal analyzer.

3. Performance

3.1. *Detection efficiency*

The overall detection efficiency of the present spectrometer was measured as a function of the X-ray energy in the following way. Powder samples of Tl_2O_3 and Bi_2O_3 were mounted on the sample holder and irradiated with 115 keV X-rays. The energy spectra of $K\alpha_1$, $K\alpha_2$, $K\beta_1$ and $K\beta_2$ fluorescence lines of these elements were measured using the spectrometer. At the same time, the spectra were also measured by the SSD2 placed 1 m apart from the sample at the same angle as the crystal analyzer. The incoming X-rays to the SSD2 were confined to a diameter of 2 mm by placing in front of it a Ta plate with a hole. A 5 mm-thick Cu plate was also attached to the Ta plate to adjust the flux of the fluorescent X-rays for the SSD2. For each fluorescence line, the integrated intensity measured by the spectrometer was compared with that by the SSD2. Fig. 6 shows the results. Here, the correction for the energy-dependent detection efficiencies of the SSDs and the absorption by the Cu filter plate are made.

3.2. *Momentum resolution*

The energy resolution of the spectrometer $\Delta\omega_2$ in equation (3) was evaluated as follows. We measured the energy spectrum of the Bi-$K\alpha_1$ fluorescence line at 77.1 keV. Fig. 7 shows the measured spectrum. The width of the spectrum is the resultant of convolution of the natural width of the fluorescence line and the energy resolution of the spectrometer. From the observed width of 139 eV in FWHM and the natural width of 91 eV in FWHM, we obtain 80 eV in FWHM for $\Delta\omega_2$, where we assume a Lorentzian for the fluorescence line and a Gaussian for the energy-resolution curve of the spectrometer. The natural width of the fluorescence line is evaluated from the absorption spectra at the Bi K-edge and L_{III}-edge measured at BL01B1 and BL39XU, respectively, of SPring-8. From the present bandwidth of the monochromator, $\Delta\omega_1$ = 113 eV, we have obtained the overall experimental momentum resolution of 0.10 a.u. It is summarized with the contributions from $\Delta\omega_1$, $\Delta\omega_2$ and $\Delta\theta$ in Table 1.

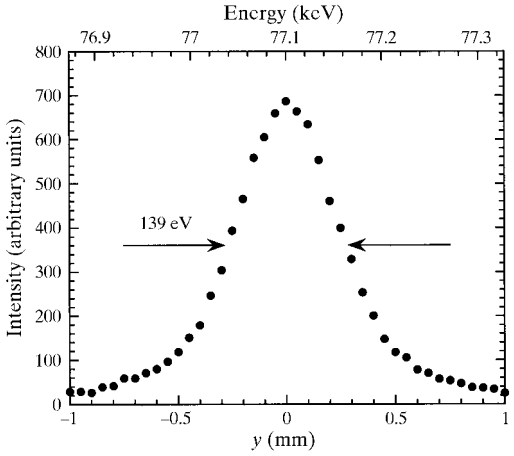

Figure 7
Energy spectrum of the Bi-$K\alpha_1$ line measured using the spectrometer. From the width of the measured spectrum and the natural width of the fluorescence line, we obtain 80 eV in FWHM for the energy resolution of the spectrometer.

3.3. *Compton profile*

To demonstrate the performance of the spectrometer, we measured the Compton profile of a single crystal of Nb along the [100] direction. Its thickness was 2 mm. The quasi-PSD was moved by about 90 mm to scan the whole profile. We should note here that the slits cover different energy ranges because they are placed at an interval of 10 mm. These ranges correspond to −13.0 to +7.9, −11.2 to +10.7, −9.3 to +13.5– and −7.1 to +16.4 a.u. in the momentum scale. Figs. 8(*b*)–8(*d*) show the energy spectra of SSD1 at some typical positions. The spectra consist of four sharp peaks and the broad background noise. The signals, namely the diffracted X-rays, can be easily separated from the noise.

The measured profile as a function of the slit position was first converted to the energy profiles and then corrected for the absorption in the sample, the scattering cross-section, the relative detection efficiency and the multiple scattering. Finally, it was converted to the momentum scale using equation (2). Fig. 8(*a*) shows the corrected and the raw profiles. Neither parasitic peak nor glitch is observed in the profile. The counting rate was 30 counts s^{-1} at the Compton peak. Counting rates at the Compton peak were also measured for another set-up of the spectrometer: a combination of 2 mm-thick crystals as the analyzer and 400 µm-wide and 4 mm-high slits in the quasi-PSD. We obtained 200 counts s^{-1} from 2 mm-thick Nb and 480 counts s^{-1} from 3 mm-thick Cu crystal, while the overall experimental momentum resolution was 0.15 a.u.

4. Summary and conclusions

We have designed and constructed an X-ray spectrometer for Compton scattering experiments using 90–120 keV X-rays at BL08W of SPring-8. The overall momentum resolution of 0.10 a.u. is the highest ever achieved for 115 keV incident X-rays. This resolution encourages us to study Fermiology and its related issues on heavy-element metals and alloys, like high-T_c superconductors and 4*f*/5*f*-heavy fermion systems. The triply layered bent crystal has successfully managed to enhance the counting rate while keeping the same energy resolution as that of the one-crystal case. Furthermore, the use of the Ge-SSD with four slits enables us to obtain energy profiles of Compton-scattered X-rays with very little noise. A Compton profile of Nb was measured with a counting rate of 30 counts s^{-1} at the Compton peak. The data-acquisition efficiency is not high, since the spectrometer sees only four p_z points at one time. The introduction of a multi-element Ge SSD, instead of the present four-slits SSD system, could improve the efficiency.

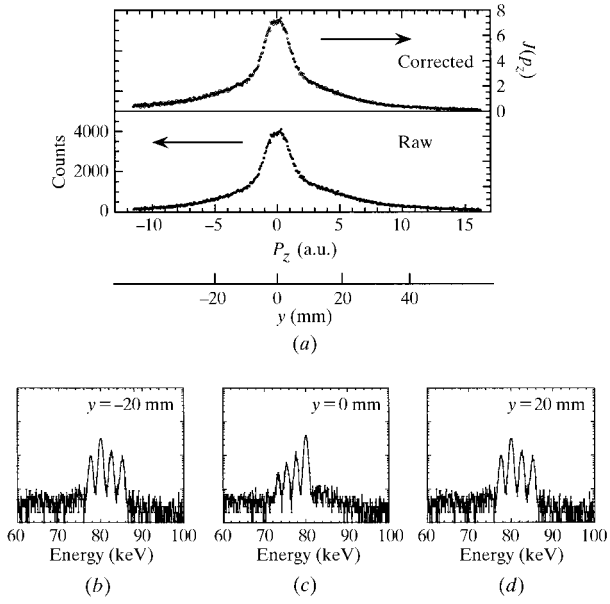

Figure 8
(*a*) Raw and corrected Compton profiles of Nb are shown in the lower frame and the upper frame, respectively. Energy spectra detected by SSD1 are presented at positions of (*b*) $y = -20$ mm, (*c*) $y = 0$ mm, and (*d*) $y = +20$ mm.

APPENDIX *A*
Derivation of equation (5)

In Fig. 2 we find

$$\overline{FM'} = \overline{MM'}\tan(\theta_B - \chi + \alpha), \tag{10}$$

with

$$\overline{FM'} = (\rho + t)\sin\alpha + y, \tag{11}$$

$$\overline{MM'} = (\rho + t)\cos\alpha + n. \tag{12}$$

We obtain equation (5) by solving y from these equations.

APPENDIX *B*
Derivation of equation (6)

In the triangles SMO and SM_oO in Fig. 9, we find

$$(\alpha + \alpha_o) + (\beta + \beta_o) = \theta_B + \chi, \tag{13}$$

$$(\alpha_o + \beta_o) = \theta_{Bo} + \chi_o, \tag{14}$$

where β is the angle MSM_o, β_o is the angle M_oSO and α_o is the angle SOM_o. Substituting equation (14) into equation (13), we obtain the following equation,

$$\alpha = \theta_B - \theta_{Bo} + \chi - \chi_o - \beta. \tag{15}$$

Likewise, we find

$$q \sin(\beta + \beta_o) = (\rho + t) \sin(\theta_B + \chi), \tag{16}$$

$$q \sin \beta_o = \rho \sin(\theta_{Bo} + \chi_o). \tag{17}$$

Then,

$$\beta = \arcsin\left\{[(\rho + t)/q] \sin(\theta_B + \chi)\right\} - \beta_o, \tag{18}$$

$$\beta_o = \arcsin\left[(\rho/q) \sin(\theta_{Bo} + \chi_o)\right]. \tag{19}$$

By substituting (18) and (19) into (15), we obtain equation (6).

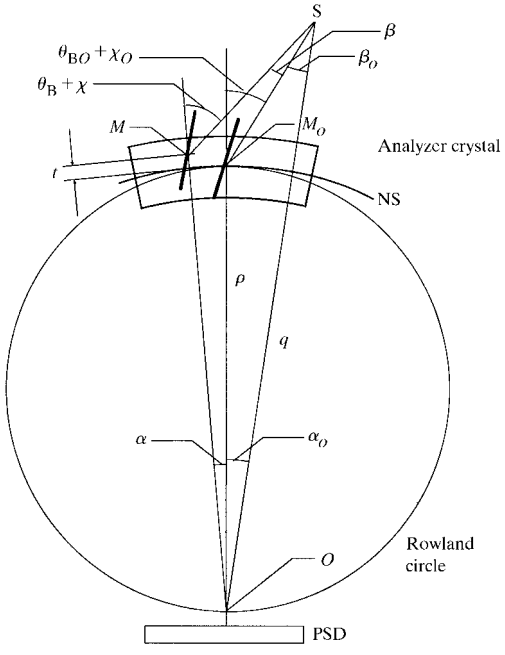

Figure 9
Focusing geometry.

APPENDIX *C*
Derivation of equations (7) and (8)

We assume that a volume element in a crystal is isotropically deformed by bending. In Fig. 10(*a*), the volume element at t from NS is expanded ($t \geq 0$) or compressed ($t \leq 0$) along the x-direction, and the strain components at t are simply expressed in the x-y Cartesian coordinates by

$$\epsilon_x = t/\rho, \tag{20}$$

$$\epsilon_y = -\nu t/\rho, \tag{21}$$

$$\gamma_{xy} = 0, \tag{22}$$

where ϵ_x and ϵ_y are normal strains, and γ_{xy} is a shearing strain. In the x'–y' Cartesian coordinates, which are rotated by χ_o, the strain components are written as

$$\epsilon_{x'} = \epsilon_x \cos^2 \chi_o + \epsilon_y \sin^2 \chi_o + (1/2)\gamma_{xy} \sin 2\chi_o, \tag{23}$$

$$\epsilon_{y'} = \epsilon_x \sin^2 \chi_o + \epsilon_y \cos^2 \chi_o - (1/2)\gamma_{xy} \sin 2\chi_o, \tag{24}$$

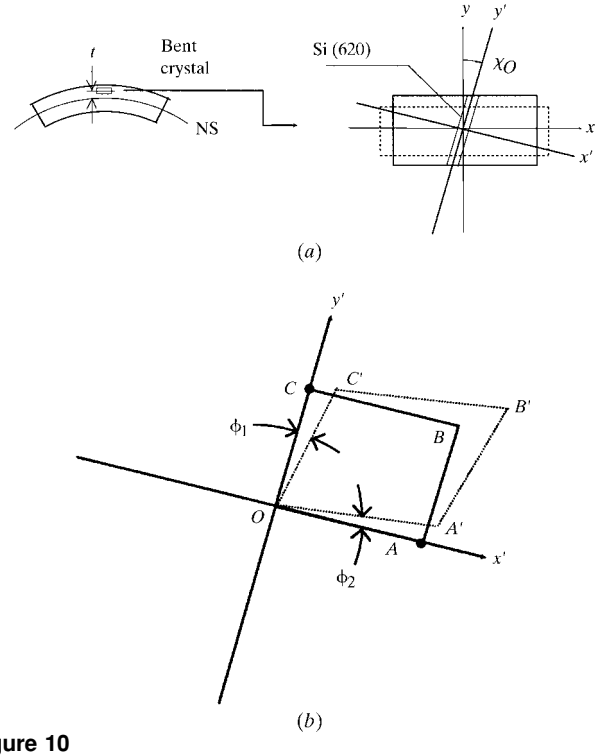

Figure 10
(*a*) Deformation of a volume element in a bent crystal. The volume element at t from NS is expanded ($t \geq 0$) or compressed ($t \leq 0$) along the x-direction of the x–y Cartesian coordinates. The x'–y' Cartesian coordinates are related to the x–y coordinates by the rotation χ_o. (*b*) Si 620 Bragg planes are rotated by ϕ_1 under the strains.

$$\gamma_{x'y'} = -(\epsilon_x - \epsilon_y)\sin 2\chi_o + \gamma_{xy}\cos 2\chi_o. \quad (25)$$

The spacing of the Si 620 planes changes to d',

$$d' = d(1 + \epsilon_{x'}). \quad (26)$$

From Bragg's law,

$$2d' \sin\theta_B = \lambda, \quad (27)$$

and with equations (20)–(23) and (26), we obtain equation (7).

The direction of the Si 620 planes is slightly rotated by ϕ_1 (see Fig. 10*b*) which is connected with $\gamma_{x'y'}$ by the following equation,

$$\phi_1 + \phi_2 = -\gamma_{x'y'}, \quad (28)$$

where ϕ_2 is the angle $A'OA$. ϕ_1 and ϕ_2 are

$$\phi_1 = (1/2)(\epsilon_x - \epsilon_y)\sin 2\chi_o + \gamma_{xy}\cos^2\chi_o, \quad (29)$$

$$\phi_2 = (1/2)(\epsilon_x - \epsilon_y)\sin 2\chi_o - \gamma_{xy}\sin^2\chi_o. \quad (30)$$

From equation (22), it is found that $\phi_1 = \phi_2$ in the present case. Then, equation (28) becomes

$$\phi_1 = -(1/2)\gamma_{x'y'}. \quad (31)$$

Consequently, the angle between the surface normal of the crystal and the Si 620 planes is given by

$$\chi = \chi_o - (1/2)\gamma_{x'y'}. \quad (32)$$

Substituting equation (25) into equation (32), we obtain equation (8).

We wish to acknowledge Professor Shiotani (Tokyo University of Fisheries), Professor Kawata (Photon Factory, KEK) and Professor Suortti (University of Helsinki) for helpful discussions and advice. We also thank Dr Uruga (JASRI) and Dr Kawamura (RIKEN) for providing the absorption spectra of Bi. One of the authors (NH) also acknowledges the support from the Junior Research Associate Program at RIKEN. This work was supported by the SPring-8 Research Promotion Scheme under the auspices of the Japan Science and Technology Corporation and performed with the approval of JASRI (proposal No. 1999-A0112-NS-np).

References

Berthold, A., Degenhardt, J., Mourikis, S., Schmitz, J. R., Schülke, W., Schulte-Schrepping, H., Wohlert, F., Hamacher, A., Protic, D. & Riepe, G. (1992). *Nucl. Instrum. Methods*, A**320**, 375–380.
Cauchois, Y. (1932). *J. Phys.* **7**, 320–336.
Eisenberger, P. & Reed, W. A. (1974). *Phys. Rev. B*, **9**, 3237–3241.
Loupias, G. & Petiau, J. (1980). *J. Phys.* **41**, 265–271.
Sakurai, Y. (1998). *J. Synchrotron Rad.* **5**, 208–214.
Sakurai, Y., Ito, M., Urai, T., Tanaka, Y., Sakai, N., Iwazumi, T., Kawata, H., Ando, M. & Shiotani, N. (1992). *Rev. Sci. Instrum.* **63**, 1190–1193.
Schulze, C., Lienert, U., Hanfland, M., Lorenzen, M. & Zontone, F. (1998). *J. Synchrotron Rad.* **5**, 77–81.
Shiotani, N., Sakai, N., Itoh, F., Sakurai, M., Kawata, H., Amemiya, Y. & Ando, M. (1989). *Nucl. Instrum. Methods*, A**275**, 447–452.
Suortti, P., Buslaps, T., Fajardo, P., Honkimäki, V., Kretzschmer, M., Lienert, U., McCarthy, J. E., Renier, M., Shukla, A., Tschentscher, Th. & Meinander, T. (1999). *J. Synchrotron Rad.* **6**, 69–80.
Suortti, P., Lienert, U. & Schulze, C. (1994). *Nucl. Instrum. Methods*, A**338** 27–32.
Suortti, P. & Thomlinson, W. (1988). *Nucl. Instrum. Methods*, A**269** 639–648.
Williams, B. (1977). Editor. *Compton Scattering.* London: McGraw-Hill.
Yamaoka, H., Hiraoka, N., Itou, M., Mizumaki, M., Sakurai, Y., Kakutani, Y., Koizumi, A., Sakai, N. & Higashi, Y. (2000). *J. Synchrotron Rad.* **7**, 69–77.
Yamaoka, H., Mochizuki, T., Sakurai, Y. & Kawata, H. (1998). *J. Synchrotron Rad.* **5**, 699–701.